Title

Epigenomic Signatures of Neuronal Diversity in the Mammalian Brain

Journal

Neuron, 86(6)

ISSN

0896-6273

Authors

Mo, Alisa
Mukamel, Eran A
Davis, Fred P
et al.

Publication Date

2015-06-01

DOI

10.1016/j.neuron.2015.05.018

Peer reviewed

NeuroResource

Neuron

Epigenomic Signatures of Neuronal Diversity in the Mammalian Brain

Highlights

- Affinity purification of nuclei in mice enables cell-type-specific epigenomics
- 3 neuron types adopt unique landscapes of DNA methylation and accessible chromatin
- Distinct TF sets are predicted to bind neuron type-specific gene regulatory regions
- A hyper-methylation signature in adult neurons captures developmental history

Authors

Alisa Mo, Eran A. Mukamel, Fred P. Davis, ..., Sean R. Eddy, Joseph R. Ecker, Jeremy Nathans

Correspondence

ecker@salk.edu (J.R.E.), jnathans@jhmi.edu (J.N.)

In Brief

Mo et al. develop a broadly applicable tool to purify genetically labeled nuclei in mice and, using genome-wide maps of gene expression, DNA methylation, and chromatin accessibility, show how three neuronal subtypes adopt distinct epigenomic configurations associated with function and development.

Accession Numbers

GSE63137

Mo et al., 2015, Neuron *86*, 1369–1384
June 17, 2015
http://dx.doi.org/10.1016/j.neuron.2015.05.018

CellPress

Neuron
NeuroResource

Epigenomic Signatures of Neuronal Diversity in the Mammalian Brain

Alisa Mo,[1,2,11] Eran A. Mukamel,[3,4,11] Fred P. Davis,[5,11] Chongyuan Luo,[6,11] Gilbert L. Henry,[5] Serge Picard,[5] Mark A. Urich,[6] Joseph R. Nery,[6] Terrence J. Sejnowski,[3,7,8] Ryan Lister,[6,9] Sean R. Eddy,[5] Joseph R. Ecker,[6,8,*] and Jeremy Nathans[1,2,10,*]
[1]Department of Molecular Biology and Genetics
[2]Department of Neuroscience
Johns Hopkins University School of Medicine, Baltimore, MD 21205, USA
[3]Computational Neurobiology Laboratory, The Salk Institute for Biological Studies, La Jolla, CA 92037, USA
[4]Department of Cognitive Science, University of California San Diego, La Jolla, CA 92037, USA
[5]Janelia Research Campus, Howard Hughes Medical Institute, Ashburn, VA 20147, USA
[6]Genomic Analysis Laboratory, The Salk Institute for Biological Studies, La Jolla, CA 92037, USA
[7]Division of Biological Sciences, University of California at San Diego, La Jolla, CA 92037, USA
[8]Howard Hughes Medical Institute, The Salk Institute for Biological Studies, La Jolla, CA 92037, USA
[9]The ARC Centre of Excellence in Plant Energy Biology, The University of Western Australia, Crawley, Western Australia 6009, Australia
[10]Howard Hughes Medical Institute, Johns Hopkins University School of Medicine, Baltimore, MD 21205, USA
[11]Co-first author
*Correspondence: ecker@salk.edu (J.R.E.), jnathans@jhmi.edu (J.N.)
http://dx.doi.org/10.1016/j.neuron.2015.05.018

SUMMARY

Neuronal diversity is essential for mammalian brain function but poses a challenge to molecular profiling. To address the need for tools that facilitate cell-type-specific epigenomic studies, we developed the first affinity purification approach to isolate nuclei from genetically defined cell types in a mammal. We combine this technique with next-generation sequencing to show that three subtypes of neocortical neurons have highly distinctive epigenomic landscapes. Over 200,000 regions differ in chromatin accessibility and DNA methylation signatures characteristic of gene regulatory regions. By footprinting and motif analyses, these regions are predicted to bind distinct cohorts of neuron subtype-specific transcription factors. Neuronal epigenomes reflect both past and present gene expression, with DNA hypermethylation at developmentally critical genes appearing as a novel epigenomic signature in mature neurons. Taken together, our findings link the functional and transcriptional complexity of neurons to their underlying epigenomic diversity.

INTRODUCTION

In the mammalian brain, distinct types of neurons interact in intricate networks to govern thought, emotion, and behavior. Neurons can differ in their morphologies, synaptic connections, electrophysiological properties, neurotransmitter identities, and developmental histories. The balance of signaling across heterogeneous neurons is critical for healthy brain function, and disruptions of genes that mediate this balance are implicated in neurological and psychiatric diseases (Sullivan et al., 2012).

Neuronal diversity arises partly through spatiotemporal regulation of gene expression by regulatory regions such as promoters and enhancers. These discrete regions of DNA can be identified using epigenomic signatures, which include accessible chromatin, active histone modifications, and low levels of DNA methylation (Bird, 2002; Heintzman et al., 2007; Stadler et al., 2011; Thurman et al., 2012). Neurons undergo extensive epigenomic changes during post-natal brain development, including de novo establishment of non-CG methylation (Lister et al., 2013; Xie et al., 2012). However, the genome-wide patterns of accessible chromatin and both CG and non-CG methylation in specific neuronal subpopulations are unknown. We reasoned that neuronal epigenomic landscapes should mirror neuronal diversity. Whereas gene expression analysis provides a snapshot of a neuron's molecular activity at a single point in time, the complementary epigenomic information captures gene regulatory mechanisms, developmental origins, and potential future responses induced by neuronal activity.

Cellular diversity is important for brain function, but it also poses a technical challenge for epigenomic studies. Cell-type-specific molecular profiling requires the isolation of targeted cell populations from complex tissues (Maze et al., 2014). Manual sorting (Sugino et al., 2006) and laser capture microdissection (Emmert-Buck et al., 1996) are useful for isolating small numbers of cells but do not provide enough material for epigenomic studies. Fluorescence-activated cell sorting (FACS) can isolate larger numbers of cells but may be challenging in tissues such as the adult brain, where cells are morphologically complex and densely interconnected. Although improvements have been made (Saxena et al., 2012), the neuronal dissociation process may also induce cellular stress

responses and perturb subsequent molecular profiles. Genetically directed strategies that isolate RNA from specific cell populations in mice (Doyle et al., 2008; Gay et al., 2013; Heiman et al., 2008; Sanz et al., 2009) have begun to chart transcriptional diversity across cell types but cannot profile epigenomic features unless combined with FACS (Mellén et al., 2012). Although nuclei can be isolated by FACS for epigenomic studies (Jiang et al., 2008), FACS-sorted nuclei are fragile and difficult to concentrate into the small volumes that are optimal for chromatin assays. An alternate approach is INTACT (isolation of nuclei tagged in specific cell types; Deal and Henikoff, 2010), which uses affinity purification to isolate tagged nuclei. Captured nuclei can be used for gene expression, epigenomic, and proteomic profiling (Amin et al., 2014; Henry et al., 2012; Steiner et al., 2012).

Here, we present the first application of INTACT in a mammalian organism and use it to address the cell-type-specific neuronal epigenome. Our approach uses the Cre-loxP system in mice to express a tagged nuclear membrane protein, allowing affinity purification of labeled nuclei from genetically defined cell populations. In this study, we applied INTACT to examine the core transcriptional and epigenomic features of three major functional classes of neocortical neurons: excitatory pyramidal neurons, Parvalbumin (PV)-expressing fast-spiking interneurons, and Vasoactive intestinal peptide (VIP)-expressing interneurons. 70%–85% of cortical neurons are excitatory. The remaining 15%–30% are inhibitory neurons, with approximately 40% expressing PV and 12% expressing VIP (Gelman and Marín, 2010; Rudy et al., 2011). Together, these mutually exclusive cell types represent both glutamatergic (excitatory) and GABAergic (inhibitory) signaling. Neocortical pyramidal neurons provide the long-range excitatory output of the brain, and inhibitory neurons modulate the rate and temporal structure of this network output (Molyneaux et al., 2007; Rudy et al., 2011). PV and VIP neurons have distinct computational roles as a result of differences in their firing patterns and synaptic connections (Kepecs and Fishell, 2014).

Several studies have identified genome-wide differences in gene expression across neuronal subpopulations (Doyle et al., 2008; Molyneaux et al., 2015; Sugino et al., 2006). However, neuron subtype-specific epigenomes remain largely unexplored. We find that among excitatory, PV, and VIP neurons, global epigenomic landscapes of DNA methylation and chromatin accessibility show widespread differences. These differences reflect distinct mechanisms of gene regulation, with candidate regulators identified using transcription factor (TF) footprinting and motif analyses. Integrating epigenomes together with expression profiles, we find intragenic non-CG methylation to be particularly salient for inferring neuronal gene expression. At TF genes with cell-type-specific developmental roles, we further identify a unique pattern of DNA hyper-methylation in adult neurons that is a long-lasting epigenomic signature of transient expression during brain development. Collectively, our results provide a comprehensive view of how distinct neuronal classes adopt unique epigenomic and gene regulatory configurations that reflect both mature neuronal function as well as developmental origin.

RESULTS

Mammalian INTACT Isolates Specific Populations of Neuronal Nuclei from the Brain

To generate a mouse line for affinity purification of labeled nuclei, we tagged the C terminus of mouse SUN1, a nuclear membrane protein, with two tandem copies of superfolder GFP and six copies of the Myc epitope (SUN1-sfGFP-Myc). We targeted *Sun1-sfGFP-myc* to the ubiquitously expressed *Rosa26* locus preceded by a *CAG* promoter and a *loxP-3x polyA-loxP* transcriptional roadblock (*R26-CAG-LSL-Sun1-sfGFP-myc*) (Figure 1A). Cells expressing Cre recombinase remove the roadblock and allow transcription of *Sun1-sfGFP-myc*. We first recombined *R26-CAG-LSL-Sun1-sfGFP-myc* in all cells using *Sox2-Cre*, a germline Cre driver (Figure S1A). *Sox2-Cre; R26-CAG-LSL-Sun1-sfGFP-myc* mice are healthy and fertile with no obvious phenotypic deficits, indicating that long-term expression of the fusion protein is well tolerated.

We expressed *Sun1-sfGFP-myc* in excitatory (Exc) neurons (*Camk2a-Cre*), PV interneurons (*PV-Cre*), and VIP interneurons (*VIP-Cre*) (Figure 1B and Table S1). Immunohistochemistry targeting GFP showed that the SUN1 fusion protein is localized to the nuclear periphery. Quantification of labeled nuclei together with neuronal markers (Figures 1B and S1B–S1G) indicated that each Cre driver predominantly recombines the targeted cell type. The pattern of labeling using anti-Myc is identical to anti-GFP (Figure S1H).

We next developed an affinity purification method to capture GFP+/Myc+ nuclei from fresh tissue homogenates (Figure 1C). Either anti-GFP or anti-Myc antibodies, together with Protein G-coated magnetic beads, can be used to isolate nuclei from both rare and common cell types with high yield and specificity. Examination of input versus affinity-purified (anti-GFP) nuclei (Figure 1D) by fluorescence microscopy showed that INTACT achieves >98% purity with >50% yield, even for cell types that represent only 1%–3% of the starting tissue (Figure 1E). Similar results were obtained using anti-Myc (95%–98% purity with 42%–65% yield, n = 3). To further assess the specificity of mouse INTACT, we performed flow cytometry on input and affinity purified (anti-Myc) nuclei from *VIP-Cre; R26-CAG-LSL-Sun1-sfGFP-myc* mice (Figure S1I). Flow cytometry showed that more than 99% of input nuclei (after step 2 in Figure 1C) were singlets, corresponding to well-isolated nuclei, and 1.5% of input nuclei were GFP+. In contrast, 98.9% of affinity purified nuclei were GFP+. Similar results were obtained using anti-GFP (Figure S1J). Therefore, both manual quantification and flow cytometry indicate that mouse INTACT isolates highly pure preparations of tagged nuclei.

INTACT RNA-Seq Captures Neuronal Subtype Markers

To assess patterns of gene expression and DNA methylation in distinct neuronal subtypes, we used RNA-seq to profile transcript abundance from INTACT-purified nuclei in adult mice, and we used MethylC-seq to generate single-base resolution methylome maps (Lister et al., 2008) from the same cell types, with the caveat that bisulfite sequencing does not differentiate between methylcytosine (mC) and hydroxymethylcytosine (hmC) (Figure 2A). RNA-seq profiles are highly similar across

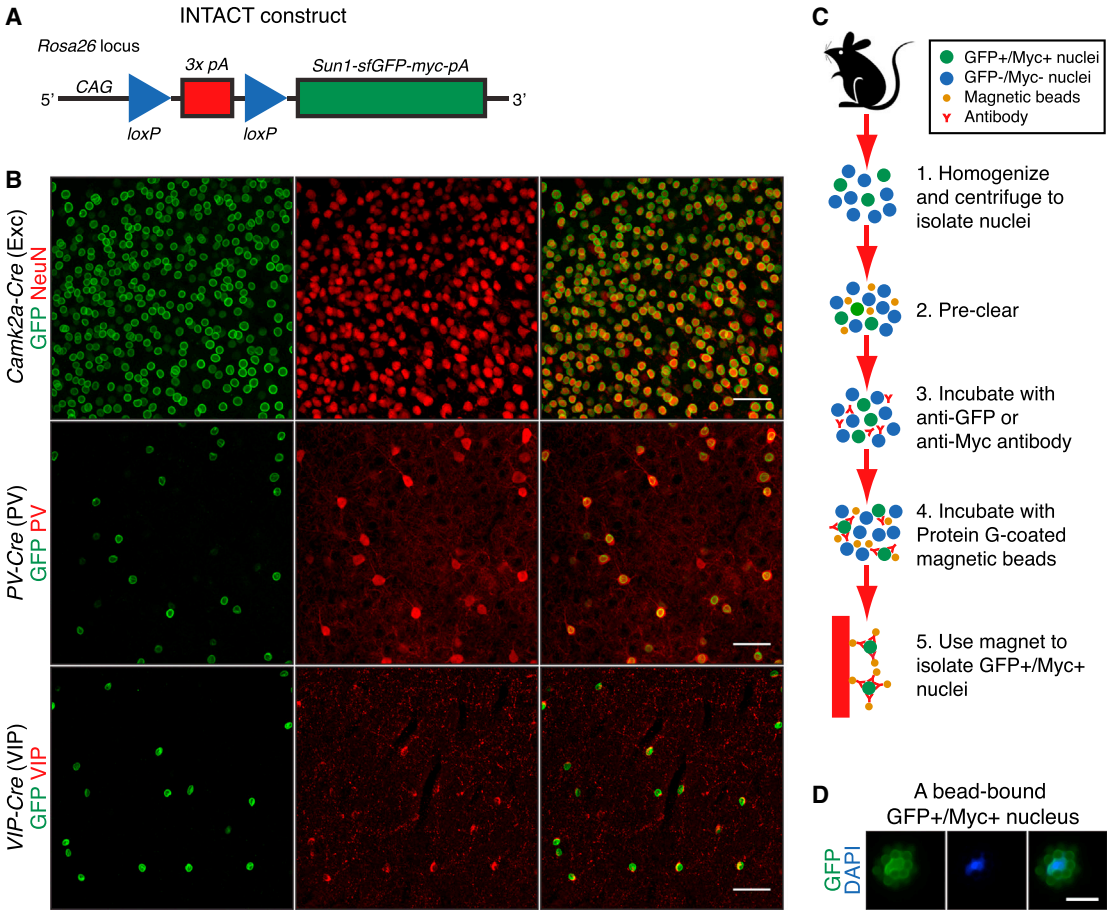

E

INTACT specificity and yield

	Input nuclei	Nuclei after INTACT purification (anti-GFP)			
Cre driver	**% GFP+**	**Specificity (% GFP+)**	**# of isolated nuclei**	**Yield**
Camk2a-Cre (n=5)	50.9%	98.5% (95.0 - 100%)	3.13 mill (1.2 - 3.7 mill)	67.6% (48.2 - 88.4%)
PV-Cre (n=4)	2.8%	98.2% (95.6 - 100%)	146,042 (83,250 - 220,150)	59.6% (38.9 - 80.0%)
VIP-Cre (n=5)	1.6%	98.6% (95.7 - 100%)	92,042 (69,000 - 100,267)	56.2% (36.9 - 74.0%)

Figure 1. An Affinity Purification Method Isolates Cell-Type-Specific Nuclei in Mice

(A) Diagram of the INTACT knockin mouse construct. Cre-mediated excision of the transcription stop signals activates expression of the nuclear membrane tag (*Sun1-sfGFP-myc*) in the cell type of interest.

(B) Immunohistochemistry showing localization of SUN1-sfGFP-Myc in neocortical excitatory, PV, and VIP neurons in mice that carry *R26-CAG-LSL-Sun1-sfGFP-myc* together with a Cre driver. Scale bars, 50 μm.

(C) Steps in the affinity purification method (INTACT).

(D) An example of a GFP+/Myc+ nucleus bound by Protein G-coated magnetic beads following INTACT purification and staining with DAPI. Scale bar, 10 μm.

(E) For each experiment, INTACT purifications were performed with anti-GFP using pooled neocortices of two mice. Specificity of mouse INTACT: after INTACT purification, bead-bound nuclei were stained with DAPI, and the numbers of GFP+ versus GFP− nuclei were quantified by fluorescence microscopy (100–200 nuclei per experiment). Yield of mouse INTACT: the total number of input nuclei, the percentage of GFP+ nuclei in the input, and the total number of bead-bound nuclei after INTACT purification were quantified using fluorescence microscopy or a hemocytometer (100–200 nuclei per experiment). The yield was calculated based on the observed number of bead-bound nuclei versus the expected number from the input. For percentage of GFP+ nuclei in the input, the mean is shown. For quantities after INTACT purification, both the mean and ranges are shown.

See also Figure S1.

replicates (r = 0.98) (Figures 2B, right panel, and S2A). A total of 4,095 genes show ≥2-fold differential transcript abundance across neuronal subtypes, with over 2,000 between each pair of neurons (Table S2). Established subtype markers are enriched in purified nuclei (e.g., *Slc17a7* and *Dkk3* in excitatory; *Pvalb* and *Lhx6* in PV; *Vip* and *Htr3a* in VIP), whereas markers of other lineages are depleted (Figure 2B, left three panels). The gene expression profile of INTACT-purified PV neurons is also

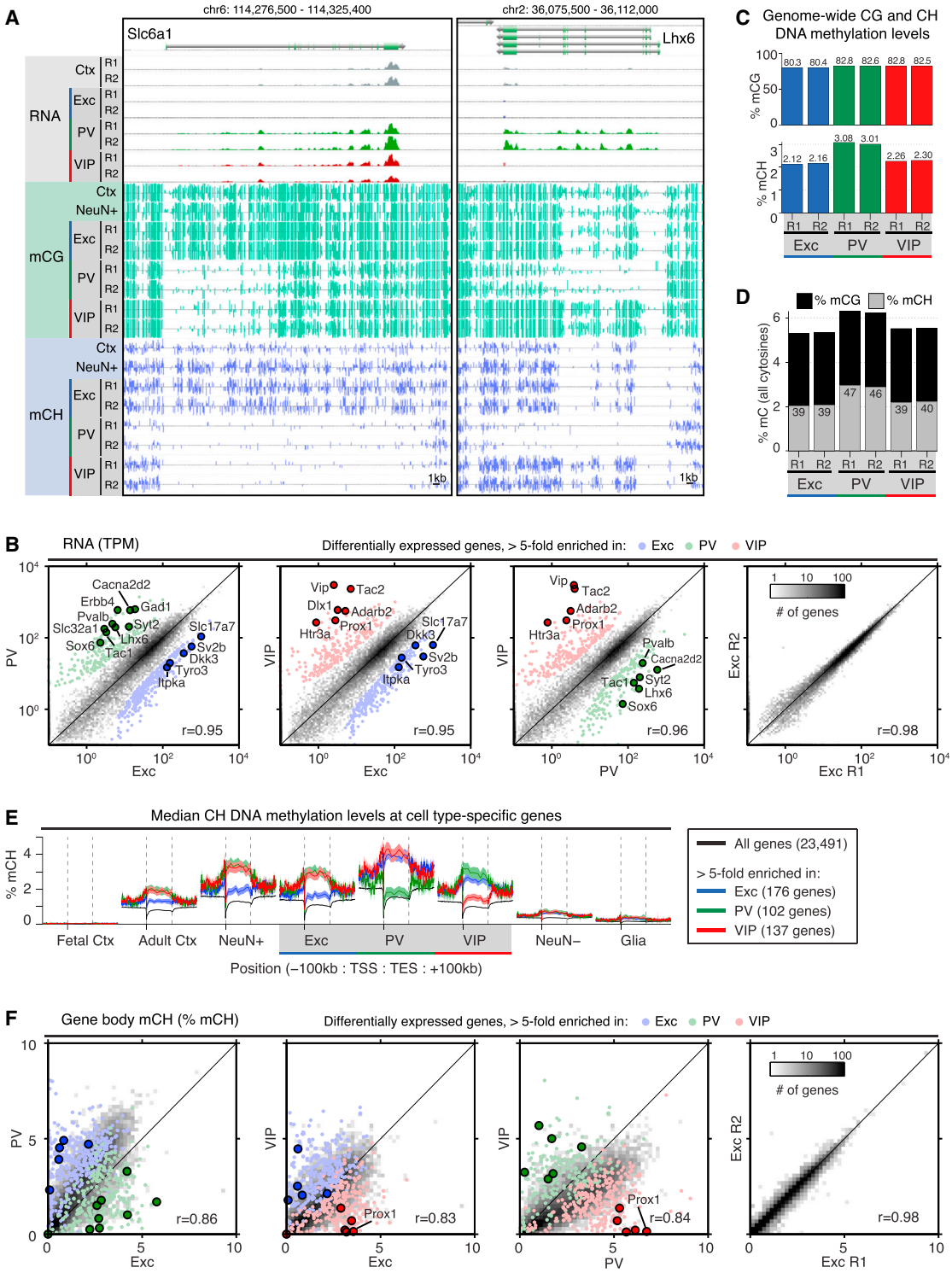

Figure 2. Widespread Differences in Gene Expression and DNA Methylation among Neuron Subtypes

(A) Browser representation of RNA-seq read density and DNA methylation in CG and non-CG contexts (mCG, mCH) at two genes. *Slc6a1* (GAT-1, left) is expressed primarily in inhibitory neurons. *Lhx6* (right) is PV neuron specific. Methylated CG (green) and CH (blue) positions are marked by upward (plus strand) and downward (minus strand) ticks. The height of each tick represents the percentage of methylation, ranging from 0% to 100%. NeuN+ and Ctx (cortex) adult mouse methylomes are from Lister et al. (2013). R1, replicate 1; R2, replicate 2.

(legend continued on next page)

consistent with RNA microarray data from manually sorted PV neurons (Figure S2B). We further used double fluorescent in situ hybridization to examine ten genes with previously unknown specificity in neocortical excitatory or PV neurons. Probe labeling for nine out of ten genes co-localized with the neuron type as predicted by RNA-seq and was excluded from other classes (Figure S2C), indicating that INTACT RNA-seq profiles identify novel patterns of gene expression.

Non-CG Methylation Is a Common Feature of Both Excitatory and Inhibitory Neurons, but Shows Widespread Differences in Genomic Distribution

In our MethylC-seq data, we observed substantial levels of DNA methylation in the non-CG context for all three neuronal populations (Figures 2A, 2C, and 2D). In most differentiated mammalian cells, DNA methylation is largely confined to the CG dinucleotide context. On the other hand, non-CG methylation (mCH, where H = A, C, or T) is a special feature of adult neurons but accumulates at much lower levels in adult glia and non-neuronal tissues (Lister et al., 2013; Xie et al., 2012). We find that mCH is most abundant in PV neurons (Figure 2C), where it constitutes nearly half (46%–47%) of the total methylcytosines (Figure 2D). Because mCH accumulates during the first weeks of post-natal development, coincident with the period of rapid synaptogenesis and long after excitatory and inhibitory lineages have diverged (Guo et al., 2014; Lister et al., 2013), these data suggest that a high level of non-CG methylation is a shared distinction of mature cortical neurons. Furthermore, because all three neuron subtypes share similar motif preferences for mCH, with CAC showing the highest methylation level (Figure S2D), it is likely that a common enzymatic mechanism (Gabel et al., 2015; Guo et al., 2014) is responsible for mCH deposition and maintenance in these neurons.

Both promoter and intragenic DNA methylation in CG and CH contexts inversely correlate with gene expression in the mammalian brain (Lister et al., 2013; Xie et al., 2012). However, a lack of cell-type specificity in existing in vivo datasets can complicate the interpretation at individual genes. For example, *Slc6a1* (GAT-1, primarily expressed in inhibitory neurons) and *Lhx6* (a PV-specific TF) appear to be both actively transcribed and highly methylated in samples of whole cortical tissue and in mixed neurons (NeuN+) (Figure 2A). Our datasets from INTACT-purified nuclei resolve these conflicting signals by showing that active gene expression and DNA methylation do not occur in the same cells but rather in distinct subpopulations. Using a list of highly specific genes from our RNA-seq data, we find that both intragenic and promoter levels of CH (Figure 2E) and CG (Figure S2E) methylation are higher in the non-expressing cell type.

DNA methylation levels in gene bodies are highly variable across neuronal subtypes. As measured by pairwise Pearson correlations (Figures 2B, 2F, S2A, and S2F–S2H), gene body mCH levels are more divergent ($r = 0.83–0.86$) than both gene expression levels ($r = 0.95–0.96$, $p = 0.003$, t test) and mCG levels ($r = 0.93–0.94$, $p = 0.001$), whereas biological replicate signals are nearly identical for all features ($r \geq 0.97$). After normalization to adjust for the genome-wide average level of mCH, 8,662 genes (38%) show >50% difference in intragenic mCH in at least one pairwise comparison of cell types, versus 6.1% between biological replicates (Figure S2I, top). Certain genes display notably higher differences. For example, the VIP-specific TF *Prox1* has 23-fold higher mCH in excitatory neurons and 32-fold higher mCH in PV neurons compared to VIP neurons (Figure 2F). Variability in gene body CH methylation is paralleled by extensive differences at a global scale (Figure S2I, bottom). Genome-wide, 37% of all 5 kb bins show >50% difference in mCH between at least one pair of cell types, compared to only 3.8% between biological replicates.

Neuronal Regulatory DNA Is Predominantly Cell Type Specific

Localized regions of accessible chromatin and low levels of DNA methylation are well-established signatures of *cis*-regulatory elements such as promoters and enhancers (Neph et al., 2012; Stadler et al., 2011; Thurman et al., 2012). Therefore, we mapped the locations of putative gene regulatory regions in specific neuronal subtypes by systematically identifying these two features (Figures 3A and S3A). In excitatory neurons, we also profiled histone modifications using chromatin immunoprecipitation (ChIP) followed by sequencing to identify potential promoters (marked by H3K4me3), enhancers (H3K4me1 and H3K27ac), and Polycomb-associated repressed regions (H3K27me3). A limitation of our analysis is that we generally did not factor in sequence variation across mouse strains, which could potentially affect mapping to the C57BL/6 reference genome as well as levels of chromatin accessibility and DNA methylation (but see Supplemental Experimental Procedures).

We identified 322,452 discrete peaks of chromatin accessibility (median length 501 bp) in excitatory, PV, and VIP neurons using sub-nucleosomal (<100 bp) reads resulting from in vitro transposition of native chromatin by Tn5 transposase (ATAC-seq, Buenrostro et al., 2013) (Table S3). We find that most

(B) Pairwise comparisons of protein-coding gene expression measured by RNA-seq across cell types (left three panels) or between replicates (right panel). The most differentially expressed genes (>5-fold change) are shown as colored points, and selected cell-type-specific genes are labeled. r, Pearson correlation of log(TPM+0.1); TPM, transcripts per million.

(C) Percentage of MethylC-seq calls supporting methylation in the CG and CH contexts for each cell type on autosomes.

(D) Percentage of all MethylC-seq calls supporting methylation. The number in each bar indicates the percentage of all methylated cytosines on autosomes that occur in the CH context.

(E) Median ± 1 SEM of percentage of mCH within and surrounding gene bodies, showing an inverse correlation between expression and DNA methylation at differentially expressed genes identified from our RNA-seq data (>5-fold change for one cell type relative to both of the other cell types). TSS, transcription start site; TES, transcription end site; SEM, standard error of the mean.

(F) Pairwise comparisons of gene body percentage of mCH across cell types (left three panels) or between replicates (right panel). Colored dots correspond to the same genes shown in (B).

See also Figure S2.

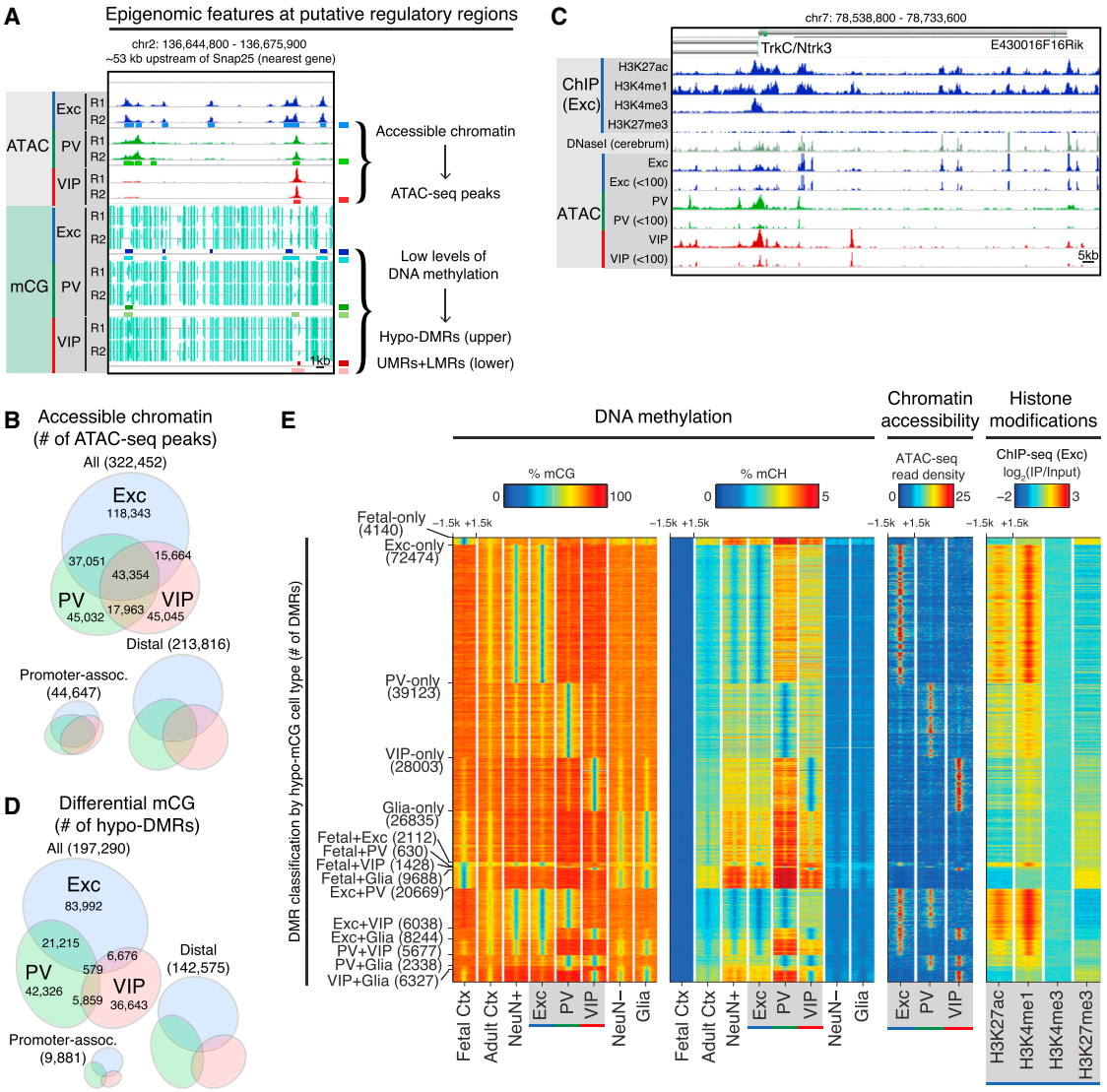

Figure 3. Epigenomic Marks Are Coordinated and Highly Cell Type Specific

(A) Examples of intergenic regulatory elements marked by accessible chromatin (peaks in ATAC-seq read density, upper tracks) and low levels of DNA methylation (hypo-DMRs and UMRs+LMRs, lower tracks) at an intergenic region ~53 kb upstream of *Snap25* (both the nearest gene and the nearest TSS). Locations of ATAC-seq peaks, hypo-DMRs, and UMRs+LMRs are shown below the corresponding raw data. R1, replicate 1; R2, replicate 2.

(B) Area-proportional Venn diagram showing the numbers of all cell-type-specific and shared ATAC-seq peaks across excitatory, PV, and VIP neurons (top). Area-proportional Venn diagrams showing that a greater fraction of promoter-associated peaks (within 2.5 kb of a TSS) are shared compared to distal peaks (>20 kb from a TSS), which are predominantly cell type specific (bottom).

(C) Browser representation of regulatory elements around *trkC/Ntrk3* marked by histone modifications in excitatory neurons, DNaseI hypersensitivity in whole cerebrum (from ENCODE), and peaks in ATAC-seq read density in excitatory, PV, and VIP neurons. For ATAC-seq, greater spatial resolution is achieved by using reads <100 bp in length (tracks labeled < 100).

(D) Area-proportional Venn diagram showing the numbers of DMRs identified to be hypo-methylated in excitatory, PV, and/or VIP neurons in a statistical comparison of CG methylation levels across five cell types. Two of these cell types, fetal cortex and glia, are not shown in the diagram. Most DMRs are distal to the TSS rather than promoter associated.

(E) Heatmap showing percentage of mCG plotted in 3 kb windows centered at DMRs hypo-methylated in one or two cell types (panel 1). At the same genomic regions, the following additional features were plotted: percentage of mCH (panel 2), chromatin accessibility (ATAC-seq reads) (panel 3), and histone modification ChIP-seq reads in excitatory neurons (panel 4). The number of DMRs in each category is shown in parentheses.

See also Figure S3.

regulatory elements in neuronal cells are cell type specific, including the large majority of distal regulatory elements (Figure 3B). In total, only 13.4% (43,354) of ATAC-seq peaks are shared across all three neuronal subtypes. Compared to DNaseI-seq data from the whole cerebrum (Stamatoyannopoulos et al., 2012), nearly all (93%) shared ATAC-seq peaks are

also detected as cerebrum DNaseI-seq peaks (Figure 3C). In striking contrast, 62% of VIP-specific, 52% of PV-specific, and 31% of excitatory-specific ATAC-seq peaks are missed in the DNaseI-seq data, highlighting the advantage of INTACT profiling over whole-tissue analysis for identifying regulatory regions, particularly those unique to sparse cell types.

We next determined regions that differ in their levels of CG methylation across five cell populations: INTACT-purified excitatory, PV, and VIP neurons, plus fetal embryonic day 13 (E13) frontal cortex and adult S100b+ glia from Lister et al. (2013). We expected that including purified neurons would facilitate identification of differentially methylated regions (DMRs). Using a conservative statistical approach (Lister et al., 2013), we identified 251,301 DMRs with a median length of 275 bp (Table S3). Masking sequence variants across mouse strains did not substantially alter the DMR calling (see Supplemental Experimental Procedures). 112,462 of these DMRs are hypo-methylated (hypo-DMRs) in excitatory neurons. In keeping with our expectation, substitution of a mixed neuronal sample (NeuN+) with comparable sequencing coverage for the excitatory neuron sample results in 77,417 (68.8%) hypo-DMRs in NeuN+ neurons, despite the prevalence of excitatory neurons in this sample. The increased detection of DMRs using INTACT-purified excitatory neurons again demonstrates the power of cell-type-specific profiling for comprehensive identification of regulatory regions. To identify hypo-methylated regions that may not be differentially methylated across cell types, we segmented each methylome into unmethylated regions (UMRs) and low-methylated regions (LMRs) (Burger et al., 2013) (Table S3).

As expected from previous studies (Stadler et al., 2011), the majority of UMRs are located at promoters (66.3%–74.2% within 2.5 kb of a TSS), whereas most LMRs are potential distal regulatory elements (4.9%–6.2% within 2.5 kb of a TSS). For DMRs, the vast majority (93.8%) are also located more than 2.5 kb away from a TSS. Across DMRs that show hypo-methylation in at least one INTACT sample (Figure 3D), between 36,643 and 83,992 are hypo-methylated in a single neuron subtype. Recapitulating the division of ATAC-seq peaks (Figure 3B), excitatory neurons have the highest number of hypo-DMRs (Figure 3D), and remarkably, most are not shared with PV or VIP neurons. Taken together, these data extend previous profiling experiments in the brain, first by identifying hundreds of thousands of putative regulatory regions across three neuron subtypes, and then by classifying them into highly distinct sets in individual subtypes.

Cell-Type Specificity at Activity-Induced Transcription Factor Binding Sites

Because regions bound by activity-dependent TFs, as a whole, show constitutive DNA hypo-methylation (Guo et al., 2011) and chromatin accessibility (Malik et al., 2014), DMRs and differential ATAC-seq peaks could point to regulatory regions with cell-type-specific responses to induced neuronal activity. Therefore, we addressed the relationship between DMRs, differential ATAC-seq peaks, and activity-dependent TF binding in excitatory neurons, reasoning that our overall findings would also be applicable to the two inhibitory subpopulations that are not easily obtainable in quantities required for TF ChIP-seq. We examined activity-dependent TF binding profiles using previously published ChIP-seq data from cortical cultures largely composed of immature excitatory neurons (Kim et al., 2010; Malik et al., 2014). The majority of activity-dependent binding sites for all TFs (58.2%–83.9%) overlap with excitatory neuron UMRs+LMRs (Figure S3B, left). However, only 1.4% of CREB and 10.8% of SRF binding sites overlap with excitatory neuron-specific hypo-DMRs, compared to 33.4%–40.3% of AP-1 (FOS, FOSB, JUNB) and NPAS4 binding sites ($p < 2 \times 10^{-38}$, Fisher's exact test [FET]). In particular, activity-dependent binding sites for AP-1 factors and NPAS4 in cortical cultures are enriched in excitatory hypo-DMRs and depleted in PV-, VIP-, and glia-specific hypo-DMRs (Figures S3B and S3C). These results are largely recapitulated by the ATAC-seq data. Our analysis suggests that excitatory neuron-specific hypo-DMRs and ATAC-seq peaks overlapping AP-1 and NPAS4 binding sites are a set of candidate regions that coordinate activity-dependent responses unique to excitatory neurons. Likewise, hypo-DMRs and differential ATAC-seq peaks in PV and VIP neurons provide a resource for identifying AP-1 and NPAS4 targets that orchestrate distinct activity-dependent responses in inhibitory neurons (Spiegel et al., 2014).

Neuronal Subtypes Show Coordinated Epigenomic Differences

Epigenomic marks carry information about cell function, via their correlation with gene expression and gene regulatory regions, as well as cell development (Bird, 2002; Hon et al., 2013; Stadler et al., 2011; Thurman et al., 2012). Therefore, we first assessed whether the epigenomic marks were well correlated with each other and then quantified their relationships across cell types and developmental stages.

Cell-type-specific hypo-methylation in the CG context is coordinated with hypo-methylation in the CH context (Figures 3E, left two panels, and S3D) and increased chromatin accessibility (Figure 3E, third panel). Excitatory neuron hypo-DMRs are also enriched for histone modifications associated with active enhancers (H3K4me1 and H3K27ac) but not promoters (H3K4me3) (Figure 3E, right panel). Similarly, ATAC-seq levels in excitatory neurons are correlated with both H3K4me1 and H3K27ac at enhancers (Figure S3E) but demarcate TF binding sites with greater spatial resolution (Figure 3E, third panel versus right panel). Overlapping features derived from multiple assays (Figure S3F) provide convergent evidence for identifying candidate regulatory regions, and both raw and processed data can be explored via a web-based browser (http://neomorph.salk.edu/mm_intact/).

We quantified the epigenomic relationships across cell types in several ways: by the similarity of DNA methylation patterns in 500 bp bins genome-wide (Figure S4A) and at ATAC-seq peaks (Figures 4A and S4B), and by the similarity of Tn5 insertion densities (Figure 4B) at ATAC-seq peaks. As expected, excitatory and NeuN+ neurons are strongly correlated using DNA methylation signal at both genomic bins and ATAC-seq peaks (Pearson r ~0.9), and hierarchical clustering groups excitatory neurons with NeuN+ neurons. PV and VIP neurons cluster together, in line with their functional roles as inhibitory neurons. In contrast, excitatory and VIP neurons show the lowest similarity across INTACT-purified cell types. Unexpectedly, CG methylation levels in fetal brain and in glia correlate more strongly

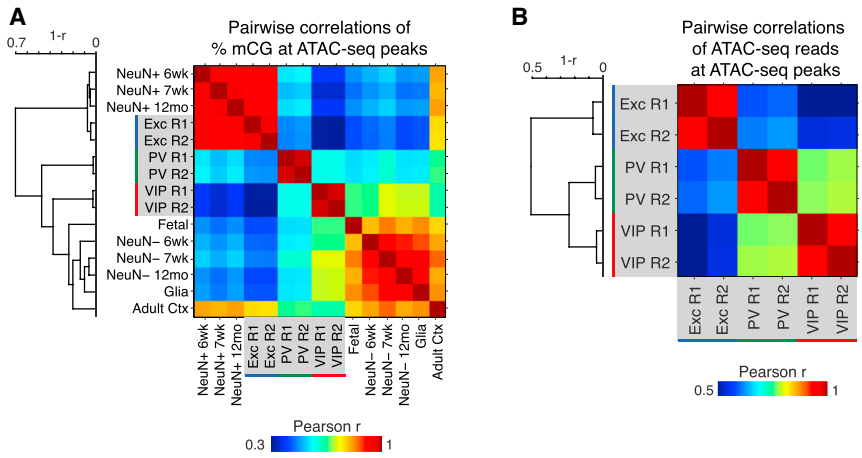

Figure 4. Relationships across Cell Types and Development via Epigenomic Marks

Matrices showing pairwise Pearson correlations for percentage of mCG (A) and ATAC-seq read densities (B) at ATAC-seq peaks. Dendrograms show hierarchical clustering using complete linkage and 1-Pearson correlation as the metric.

See also Figure S4.

with VIP neurons than with excitatory or PV neurons. At ATAC-seq peaks (Figures 4A and S4B), this similarity among VIP, fetal, and glial samples could suggest that more gene regulatory characteristics of immature or progenitor cells are retained by VIP neurons than by excitatory or PV neurons. Collectively, our data demonstrates that DNA methylation and chromatin features reveal a coordinated, hierarchical organization of mature cortical cell types that is reflected across much of the genome.

Distinct Sets of DNA Binding Factors Act at Putative Neuron Subtype-Specific Regulatory Regions

We next sought to characterize the DNA binding TFs that are responsible for these unique neuronal regulatory landscapes. Our RNA-seq analysis identified 267 differentially expressed TFs (Table S2). These include TFs that play well-known regulatory roles in the development of each cell type (e.g., *Lhx6* in PV interneurons and *Prox1* in VIP interneurons) (Kessaris et al., 2014) as well as many other TFs with unknown neuronal functions.

TF binding enhances chromatin accessibility, but the central region of binding is protected from the activity of enzymes such as Tn5 transposase, resulting in a notch, or footprint, in the ATAC-seq profile (Buenrostro et al., 2013). In agreement with previous footprinting studies (Neph et al., 2012), we observe a range of footprint shapes for different TFs (Figure 5A). With the notable exceptions of CTCF and ZFP410, footprinted sites in a cell are generally associated with reduced regional DNA methylation levels (Figure S5A).

We applied footprint analysis of ATAC-seq datasets to infer TF binding at cell-type-specific regulatory regions and combined it with complementary analysis of DNA binding sequence motifs enriched at hypo-DMRs. We focused on footprints and motifs of moderately to highly expressed TFs (TPM $\geq$ 30) and identified 68 TFs that may regulate cell-type-specific gene expression (Figure 5B and Table S4). Overall, both our footprint and motif predictions converge on similar sets of enriched and depleted TFs. These sets encompass both well-established and novel TFs. In excitatory neurons, both footprint and motif predictions show overrepresentation of *Egr*, AP-1 family members, *Neurod2*, *Rfx1/3/5*, and *Tbr1*. Two TF groups potentially linked to PV neuron development, *Mafb/g* and *Mef2a/c/d* (Kessaris et al., 2014), are among those enriched in PV-specific footprints and hypo-DMRs (Figure 5B) as well as PV hypo-DMRs shared with both excitatory and VIP neurons (Figure S5B). Studies of MEF2 have largely focused on its role in excitatory neurons (Rashid et al., 2014); here, both footprinting and motif analyses suggest a critical function for MEF2 in PV neurons at PV-specific regulatory regions. Interestingly, VIP neuron footprints and DMRs are enriched for TFs best known for their developmental roles (e.g., *Dlx*, *Pou*, and *Sox* family members; *Arx* and *Vax2*) (Kessaris et al., 2014), an extension of our previous observation that VIP methylomes share common patterns with fetal and glial methylomes. Motifs for these TFs are also enriched at fetal and glial hypo-DMRs, including those that are shared with VIP neurons (Figure S5B).

TFs control complex cellular processes by forming networks of mutual regulation, yet differences in TF regulatory networks between neuron types are largely unknown. We examined regulatory interactions among TFs by building networks of predicted cell-type-specific TF regulation, as well as a pan-neuronal regulatory network (Figures 5C and 5D; Table S4). These networks recover a number of previously implicated TF-TF regulatory interactions and suggest novel interactions. For example, our prediction that MEF2D targets *Dlx6* in PV neurons parallels the requirement of a homolog, MEF2C, for *Dlx6* expression in branchial arches (Verzi et al., 2007).

To explore the potential contribution of ATAC-seq peaks and footprints to the regulation of nearby gene expression, we examined their coverages around the TSS of highly cell-type-specific genes. Differentially expressed genes display an increased density of cell-type-specific footprints centered around the TSS (Figure 5E) and are significantly enriched for cell-type-specific ATAC-seq peaks (Figure 5F). When we examined pan-neuronal genes (Hobert et al., 2010) such as *Pclo*, *Rims1*, *Cdh2*, and *Grip1* (Figure S5C), we noted that they were also surrounded by an array of ATAC-seq peaks, many of which were present exclusively in one neuron class. Indeed, we find that cell-type-specific ATAC-seq peaks are moderately enriched around the TSS of pan-neuronal genes (Figure 5F), highlighting the potential for these regions to shape neuronal identity by regulating both cell-type-specific and pan-neuronal programs of gene expression.

Among DNA Methylation and Chromatin Accessibility Features, Non-CG Methylation Best Correlates with RNA Abundance

Genome-wide, we find a strong inverse correlation between RNA abundance and DNA methylation around the TSS, as well as a

positive correlation between RNA abundance and ATAC-seq signals (Figure 6A). For both mCG and mCH, the inverse correlation extends throughout the gene body, with a peak ~1–2 kb downstream of the TSS. At differentially expressed genes, mCH is significantly more correlated with expression (Spearman $r = -0.50$) than mCG ($r = -0.34$; $p = 0.0063$, t test using the three cell types as samples) or ATAC-seq insertion density ($r = 0.25$; $p = 5.4 \times 10^{-4}$). A generalized linear model with a sparseness-promoting regularization (LASSO) using mCG, mCH, and ATAC-seq features (Table S5) further identifies gene body mCH as the most informative feature for inferring RNA abundance (Figures S6A and S6B).

Our finding that the strongest correlation between RNA levels and mCG occurs ~1–2 kb downstream of the TSS agrees with recent findings in medulloblastoma cell lines (Hovestadt et al., 2014) and in human cardiomyocytes (Gilsbach et al., 2014). Our results extend this observation to mCH and show that mCH, an epigenetic modification abundant across diverse classes of neocortical neurons, is better correlated with gene abundances measured by RNA-seq. Future studies using more direct measures of gene transcription are warranted to complement these findings.

Gene Clusters Based on Intragenic Non-CG Methylation Share Gene Expression, Chromatin, and Functional Organization

As described above, non-CG methylation within the gene body is inversely correlated with gene expression. Yet, this epigenomic feature may display greater divergence across neuron types than their transcriptional configurations (Figures 2B and 2F), suggesting that it contains additional information related to cell-type-specific differences. To explore this idea, we used an unbiased clustering approach to group genes by their patterns of intragenic mCH, followed by an integrative analysis of gene expression, chromatin accessibility, and gene ontology. 23,023 genes were grouped into 25 clusters by their levels of intragenic mCH, normalized by the level in the flanking region (Figures 6B–6E and S6C). Approximately half of these genes share similar patterns of mCH across neurons, including hyper-methylated genes with low expression levels (clusters 2, 6; 13.5% of genes) and hypo-methylated genes with moderate to high expression (clusters 3–5, 7, and 8; 40%). The latter category is not enriched for differentially expressed genes (Figure 6D) but is enriched for cell-type-specific ATAC-seq peaks (Figure 6E). By gene ontology (GO) analysis (Huang et al., 2009) (Table S5), genes in these clusters tend to be enriched for general cellular processes, for example, transcription (GO: 0006350) and RNA binding (GO: 0003723).

The remaining half of genes captures the spectrum of intragenic CH methylation across neuronal populations by clustering into groups showing neuron subtype-specific hyper- and hypo-mCH. Clusters 10–18 (23.6% of genes) are hyper-methylated at CH sites in one or more cell types and are expressed at relatively low levels. Clusters 19–25 (17.8% of genes) are hypo-methylated in specific cell types and are generally expressed at higher levels, with hypo-methylation occurring together with increased expression (e.g., Cluster 22 enriched for PV > Exc and VIP genes). These clusters are enriched for both differentially expressed genes and accessible chromatin. Although genes that are exclusively expressed in only one or two cell types are grouped in clusters 19–25, a subset of pan-neuronal genes that differ in their expression levels across neuronal subtypes are also grouped here (e.g., *Cdh2*, *Grip1*, *Bsn*). These clusters also contain pan-neuronal genes that do not meet our threshold for differential expression (e.g., *Anks1b*), an example of the ability of intragenic mCH to parse the neuronal transcriptome into finer patterns.

Several clusters with cell-type-specific hypo-methylation are enriched for neuronal GO categories, for example, postsynaptic density (GO: 0014069: 6.7-fold enrichment, $q = 0.035$, cluster 19) and synapse (GO: 0045202: 2.6-fold, $q = 0.033$, cluster 20; 2.9-fold, $q = 2.8 \times 10^{-4}$, cluster 21). Neuron subtype-specific differences in intragenic mCH may be especially relevant in light of recent evidence that MeCP2 binding to mCA represses transcription of long neuronal genes (Gabel et al., 2015). The enrichment of neuronal GO categories at these clusters suggests that cell-type-specific expression levels of genes with neuronal functions may partly be a consequence of differences in levels of intragenic mCH.

Non-CG Methylation Is Lowest at the Nucleosome Center and Increases at Linker Regions

In addition to its variations with gene expression, we asked whether mCH levels also differed relative to chromatin features such as nucleosome positioning. We estimated nucleosome locations using ATAC-seq and found that coherently phased modulation of mCH is evident over approximately 1 kb (~5 nucleosomes), decreasing by up to 9.5% at the nucleosome center and increasing by 11.1% in neighboring linkers (Figure 6F). mCG levels display a similar but weaker modulation (<2%) (Figure S6D). Our results support earlier studies in the CG context (Teif et al., 2014) and extend the link between nucleosome positioning and DNA methylation in mammalian cells to the non-CG context.

Identification of Distinct Classes of Large Hypo-methylated Regions

We further sought to identify multi-kilobase regions of low DNA methylation in our datasets. Hypo-DMRs are not randomly distributed in the genome but instead show a bimodal distribution of inter-DMR distances (Figure 7A). Closely spaced hypo-DMRs may represent fragments of larger hypo-methylated features. Therefore, we merged neuron subtype-specific hypo-DMRs located within 1 kb of each other and defined those exceeding 2 kb in length as "large hypo-DMRs" (Figure 7B, left). We also observed another category of large hypo-methylated domains that are consistent with previously described DNA methylation valleys (DMVs) or canyons (Jeong et al., 2014; Xie et al., 2013) (Figure 7B; see Supplemental Experimental Procedures).

Although both are multi-kilobase hypo-methylated regions, large hypo-DMRs and DMVs occupy distinct genomic locations (Figure S7A). Compared to large hypo-DMRs, DMVs have higher overlap across cell types (Figure S7A) and more extreme lengths (Figure S7B), extending up to 104 kb compared to large hypo-DMRs, which extend to 32 kb. Consistent with their higher GC content (Figure S7C) and lower levels of CG methylation

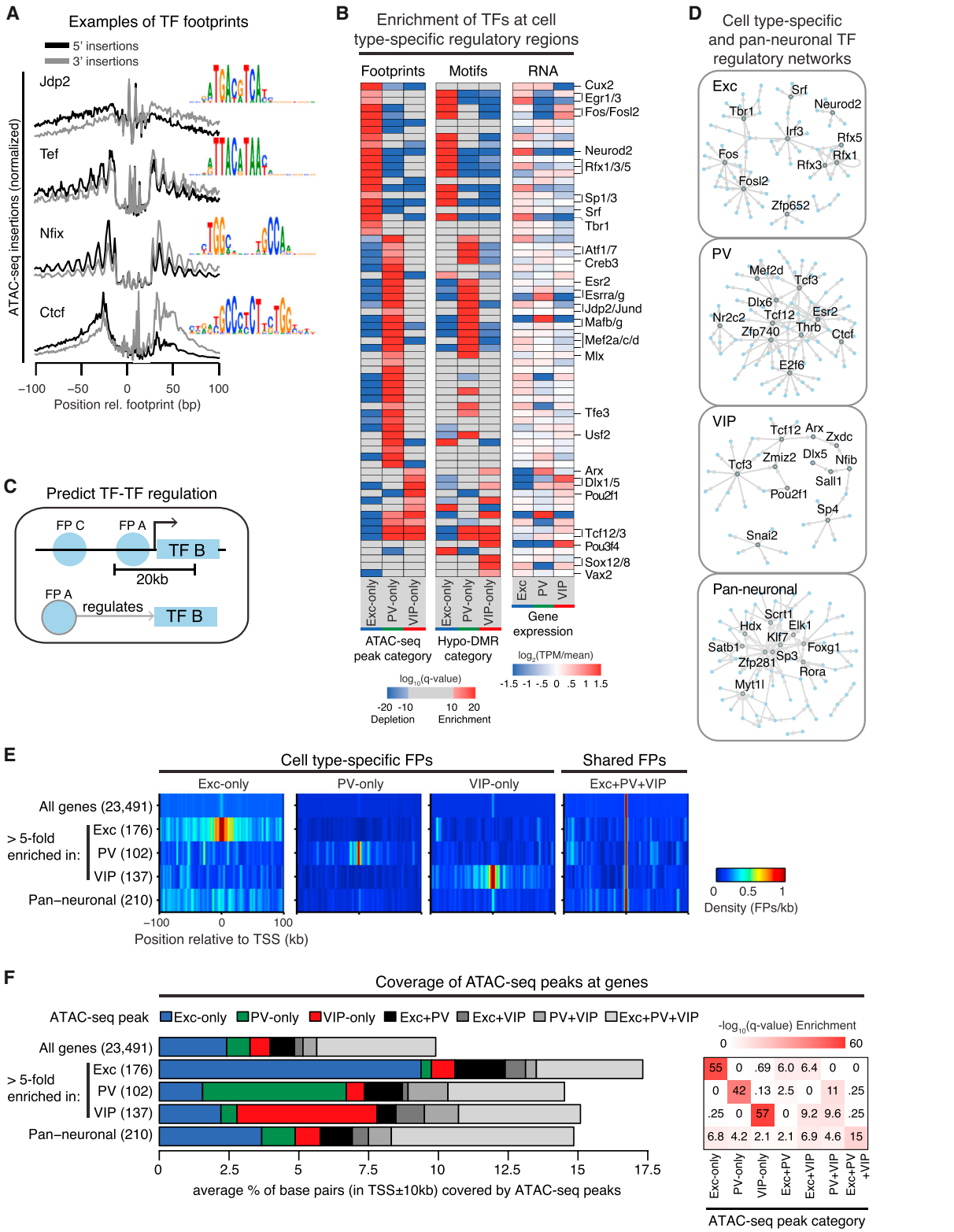

Figure 5. Neuronal Subtypes Are Associated with Distinct Patterns of TF Binding

(A) The average density of ATAC-seq read endpoints (Tn5 transposase insertions) within ±100 bp relative to the estimated locations of footprints for four example TFs, showing characteristic footprint structures. Each footprint profile is normalized by the maximum over the profiled region. Inset: position weight matrix showing sequence motifs at the footprint center.

(legend continued on next page)

(Figure S7D), most DMVs (85%–94%) overlap CpG islands. In contrast, only 1%–9% of large hypo-DMRs overlap CpG islands. Furthermore, DMVs straddle the TSS, whereas large hypo-DMRs are enriched downstream of the TSS (Figure S7E).

To better characterize different classes of hypo-methylated regions, we took advantage of our histone modification data in excitatory neurons. Large hypo-DMRs show higher levels of histone modifications associated with active enhancers, H3K27Ac and H3K4me1, compared to DMRs <2 kb (Figure 7C, left). Excitatory DMVs display a bimodal distribution for H3K4me3 and H3K27me3 and can be divided as H3K4me3+ (Figure 7B, left) versus H3K27me3+ (Figure 7B, right). As expected, H3K27me3+ DMVs are depleted for ATAC-seq reads and overlap genes with low expression (Figure 7C, middle and right). Large hypo-DMRs and H3K4me3+, but not H3K27me3+, DMVs are enriched for differentially expressed genes (Figure 7D). In fact, the bimodal distribution of H3K4me3 and H3K27me3 levels in DMVs suggests that these domains can be associated with either active or repressed genes, and the two histone modifications partition DMVs into functionally distinct categories (Figures S7F and S7G).

Hyper-methylation at Cell-Type-Specific Transcription Factor Genes Preserves a Trace of Early Developmental Expression

DMVs are highly overlapping across adult cell types and fetal cortex (Figure S7A), in line with previous evidence (Xie et al., 2013) suggesting they may be established early during development and subsequently maintained. To address whether these regions are dynamically modified during development, we compared the boundaries of fetal DMVs between fetal and adult cells. Genome-wide, 51%–67% of fetal DMVs remain as DMVs in adult neurons and glia but gain methylcytosines, resulting in a contraction of DMV length as the brain matures (median decrease = 747 bp; $p < 2 \times 10^{-18}$, Wilcoxon rank sum).

We further focused our analysis on fetal DMVs overlapping genes. Fetal DMVs are highly enriched for TF genes (Figure S7G), and 75 out of 77 fetal DMVs associated with a list of candidate developmental TFs (Visel et al., 2013) are shorter in at least one adult cell type (Figure S7H). To identify the DMVs that display the most significant developmental mCG gains, we compared mCG levels across fetal and adult cells in the interior of fetal DMVs; to avoid the possible confound of intragenic DNA methylation, we used the DMV interior upstream of the TSS (Figure 7E). This analysis identified 454 genes (66%; FET, $q < 0.01$) that exhibit significantly increased mCG in at least one adult cell type versus fetal cortex; 210 genes (31%) have more than a 5-fold increase (Table S6).

When we examined these 210 genes, we noted that several code for critical TFs known to shape neuronal subtype identity and are predominantly expressed in neural progenitor cells and immature precursors; furthermore, the highest mCG fold change generally occurs in the cell type where the gene is active in development but downregulated in the adult (Table S6). For example, *Neurog2* is highly expressed during embryonic development in the common progenitors of cortical excitatory neurons and many glial cells, but it is not expressed in these cells in the adult brain nor at any time during inhibitory neuron development (Sommer et al., 1996; Wang et al., 2013). Our DNA methylation data shows that *Neurog2* lies within a DMV in all cells except excitatory neurons and glia, where the region is hyper-methylated (Figure 7F, left). In contrast, *Nkx2-1* is specifically expressed in the medial ganglionic eminence (MGE), the birthplace of cortical PV neurons (DeFelipe et al., 2013). Immature cortical PV neurons switch off *Nkx2-1* soon after leaving the MGE in order to direct their migration to the cortex; neurons that maintain *Nkx2-1* expression instead travel to the striatum (Nóbrega-Pereira et al., 2008). An extended (>15 kb) DMV covers *Nkx2-1* in fetal cortex, excitatory neurons, VIP neurons, and glia, yet this DMV is only ~6.5 kb in PV neurons (Figure 7F, right). Similar findings are seen at DMVs overlapping *Dlx2*, *Pax6*, *Vax1*, and *Gsx2* (Figures S7I and S7J).

At these TF loci, the methylomes of adult neurons contain a signature of past gene expression. In contrast to the rest of the genome, hyper-methylation, rather than hypo-methylation, marks the relevant cell-type-specific genes. In contrast to vestigial enhancers (Hon et al., 2013), this epigenetic trace of the neuron's development arises from the gain of cell-type-specific hyper-methylation rather than the retention of hypo-methylation. We further asked what fraction of this hyper-methylation is a result of hmC rather than mC. For DMVs at *Neurog2* and *Pax6*, we find that adult frontal cortex hmCG levels from TAB-seq (Lister et al., 2013) are approximately 10% of excitatory neuron MethylC-seq signals at CG sites. Because we lack matched hmC data from purified excitatory neurons, the precise contribution of hmCG is difficult to assess, although we believe from this comparison that the majority of the hyper-methylation originates from mCG. Furthermore, at non-CG sites in these two DMVs, we find that essentially all of the observed hyper-methylation originates from mCH, consistent with evidence that hydroxymethylation occurs nearly exclusively in the CG context (Yu et al., 2012).

DISCUSSION

This study introduces the INTACT system in mice, the first method to affinity purify nuclei from genetically defined cell types

(B) Heatmaps showing the enrichment (red) and depletion (blue) of footprints in cell-type-specific ATAC-seq peaks (left) or motifs in hypo-DMRs (middle). The relative TF expression level across excitatory, PV, and VIP neurons is also shown (right). Selected TFs are labeled; the full matrix can be found in Table S4.
(C) Schematic for assessing TF-TF interactions by detecting footprints of one TF (FP A) in a 20 kb window around the TSS of a second TF (TF B); footprints located farther away (FP C) are not predicted to interact.
(D) Networks of TF interactions predicted by the method shown in (C) using cell-type-specific and pan-neuronal footprints. Full networks can be found in Table S4.
(E) Heatmaps showing the average density of cell-type-specific and pan-neuronal footprints within a TSS ± 100 kb window for each category of genes.
(F) Barplot showing the average percentage of base pairs within a TSS ± 10 kb window that overlaps each ATAC-seq peak category, for each category of genes (left). Heatmap showing an enrichment of cell-type-specific peaks at both cell-type-specific and pan-neuronal genes (right). Pan-neuronal genes are from Hobert et al. (2010); q from one-sided Wilcoxon rank-sum test with Benjamini-Hochberg FDR correction.
See also Figure S5.

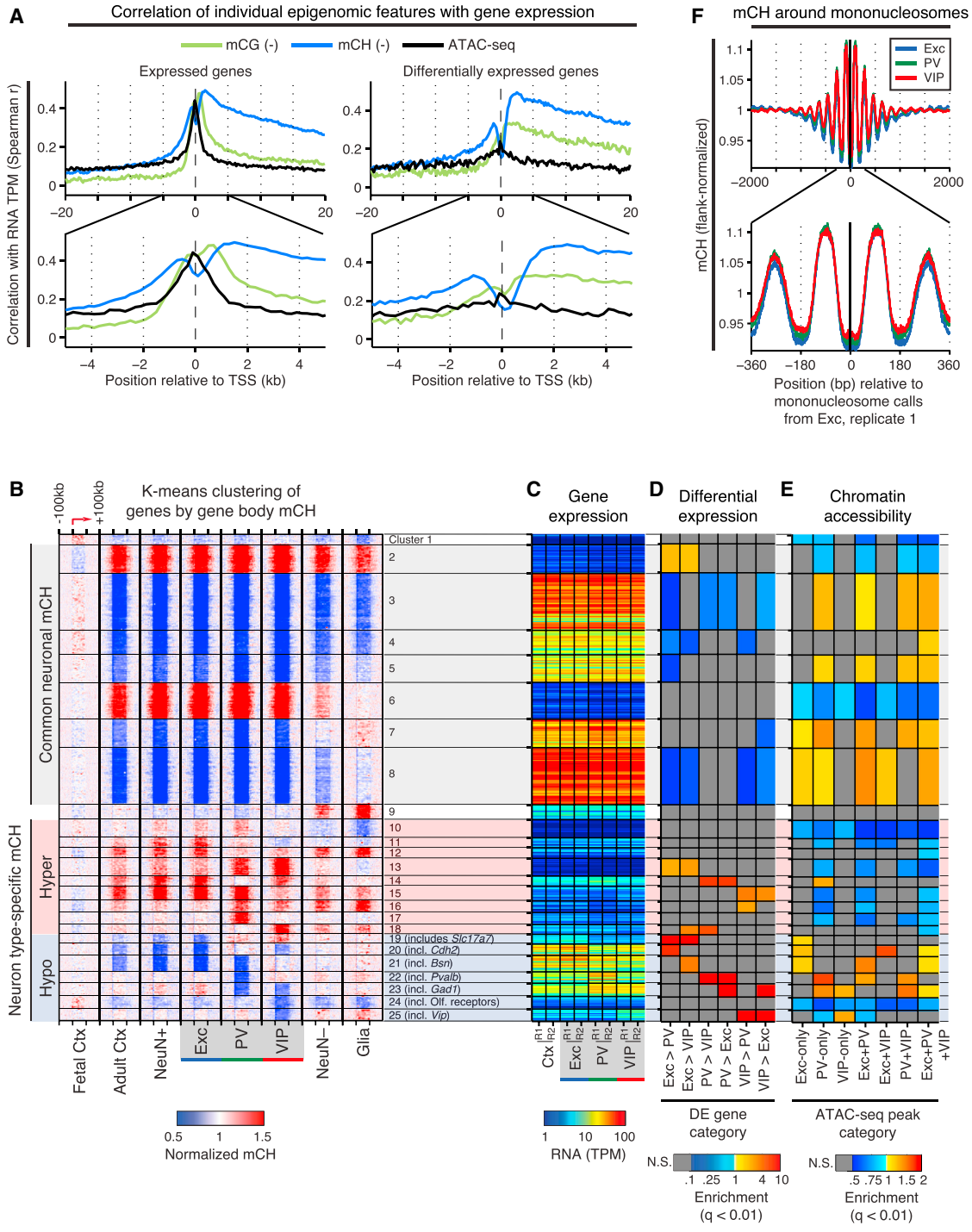

Figure 6. Integrative Analysis of DNA Methylation, Gene Expression, and Chromatin Features

(A) Spearman correlations of three epigenomic features (CG DNA methylation, CH DNA methylation, and ATAC-seq read density) with RNA expression level around the TSS of autosomal expressed (TPM > 0.1) genes (left) and differentially expressed genes (right). The signs of the correlations for mCG and mCH are negative, as these features inversely correlate with gene expression.

(B–E) Protein-coding genes were clustered by k-means based on patterns of intragenic mCH. For each cluster (1–25), the following features are plotted: mCH level within each gene body and flanking 100 kb (B); mRNA abundance (C); enrichment or depletion for differentially expressed (DE) genes (D), and enrichment or depletion for cell-type-specific and shared ATAC-seq peaks within ±10 kb of the TSS (E). mCH levels for each gene are normalized by the levels at distal flanking

(legend continued on next page)

in a mammal. INTACT efficiently isolates nuclei from both common and rare cell types, enabling us to examine the epigenomic organization of neocortical excitatory, PV, and VIP neurons with unprecedented cell-type-specific resolution. We find that the morphological and physiological diversity of neocortical neurons is paralleled by widespread differences in their underlying epigenomes. By using coordinated epigenomic marks to show that neocortical neurons adopt unique regulatory landscapes, our data add a new resource to existing catalogs of transcriptional diversity. We further identify candidate TFs acting at regulatory regions and demonstrate how epigenomic states of adult cells capture long-lasting attributes of neuronal identity, including patterns of past gene expression, current gene expression, and potential experience-dependent responses. In particular, we find a close relationship between intragenic non-CG methylation and differential gene expression. Furthermore, purified neuronal epigenomes reveal distinctive hyper-methylation patterns associated with developmentally transient expression of critical TFs that shape neuronal subtype identity.

Affinity Purification of Nuclei Facilitates Epigenomic Studies

INTACT is uniquely suited to investigating cell-type-specific epigenomes, an application that can be challenging with other purification methods. Genome-wide epigenomic assays generally require tens of thousands to millions of cells, which limit the utility of manual sorting for this purpose. Methods that involve cellular dissociation in the adult brain may be inefficient and induce stress responses that alter the cellular state. In contrast, INTACT couples rapid tissue lysis with gentle isolation of sufficient numbers of cell-type-specific nuclei for epigenomic studies. Whereas FACS-sorted cells or nuclei may be fragile and difficult to manipulate, the attachment of magnetic beads to nuclei in INTACT greatly simplifies buffer exchanges and volume reductions. Furthermore, unlike FACS or laser capture microdissection, INTACT requires no specialized instruments. INTACT is particularly well-suited for isolating rare cell types; cells constituting 1%–3% of the starting material can be enriched to >98% purity and subsequently used for MethylC-seq and ATAC-seq.

In this study, we have focused on cellular diversity in the healthy mammalian brain. INTACT can also be used to explore cell-type-specific epigenomics in mouse models of neurodegeneration, schizophrenia, autism, and other neuropsychiatric disorders or adapted for use in non-neuronal tissues. In addition to epigenomic studies, INTACT is an efficient method for isolating nuclear RNA from defined cell types that complements existing strategies for RNA profiling. We note that some degree of non-specific RNA contamination is intrinsic to affinity purification strategies, including INTACT. Nevertheless, we have shown that INTACT expression profiles recover known cell markers and can be used to discover novel markers.

Cell-Type-Specific Developmental Signatures Are Encoded in the Methylomes of Adult Cells

Mature neuronal diversity arises from a developmental odyssey. Whereas one class of large hypo-methylated regions (large hypo-DMRs) reflects the neuron's current transcriptional state, a second class (DNA methylation valleys [DMVs]) reveals patterns of past gene expression. We find that a subset of genes coding for TFs that establish neuronal identity, including *Neurog2*, *Nkx2-1*, *Dlx2*, *Pax6*, *Vax1*, and *Gsx2*, overlap with DMVs showing cell-type-specific hyper-methylation. At these genes, hyper-methylation at DMVs in the adult methylome provides a record of transient high TF expression during development, whereas the same genes are hypo-methylated in other cell types. We speculate that this pattern might arise if (1) these DMVs are initially marked by H3K27me3 in neural progenitors (Xie et al., 2013), (2) H3K27me3 is removed in a particular neuronal lineage to allow TF expression at the appropriate developmental time point, and (3) this removal simultaneously increases the accessibility of the region to DNA methyltransferases, whereas other cell types maintain an inaccessible chromatin state throughout development and into adulthood. Measuring gene expression in defined populations of immature cells can be challenging as they are intermixed and often do not express the terminal markers of adult neuronal subtypes. Our data suggest that developmental TF expression could be predicted from DNA methylation patterns in adult cells, providing an alternate approach to investigating cell-type-specific developmental history. Our results highlight this finding at several of the most critical neuronal TFs; however, future studies using matched developmental and adult datasets are necessary to further explore the temporal relationships across DNA methylation, gene expression, and chromatin.

Genome-wide Analyses Parse Neuronal Diversity

Neuronal cell types have been defined based on morphology, electrophysiology, connectivity, and, more recently, patterns of gene expression and regulation. Traditional approaches for investigating these features produce datasets of modest size and with a relatively small number of independent parameters, which limit the distinctions that can be made among neuronal cell types. As demonstrated here, genome-wide approaches generate large and information-rich datasets that reveal complex neuron subtype-specific patterns of transcript abundances, DNA methylation, and chromatin accessibility. Genome-wide information derived from these datasets can be used to parse neuronal subtypes into even finer divisions based on patterns of both gene expression and gene regulation, which in turn can be combined with transgenic approaches to label new subpopulations of neurons and enable their purification. The synergy between genetic engineering of experimental organisms, cell-type-specific purification, and genome-scale data analysis promises a new and comprehensive view of neuronal diversity in the mammalian brain.

regions (50–100 kb upstream and downstream of the gene body). For clusters with cell-type-specific hypo-methylation, an example gene or gene set is listed. TPM, transcripts per million; N.S., not significant (FET, $q < 0.01$).

(F) mCH levels are higher in the nucleosomal linker region and lower in the nucleosome core. mCH levels are normalized by the level at flanking regions (1–2 kb upstream and downstream of the nucleosome center).

See also Figure S6.

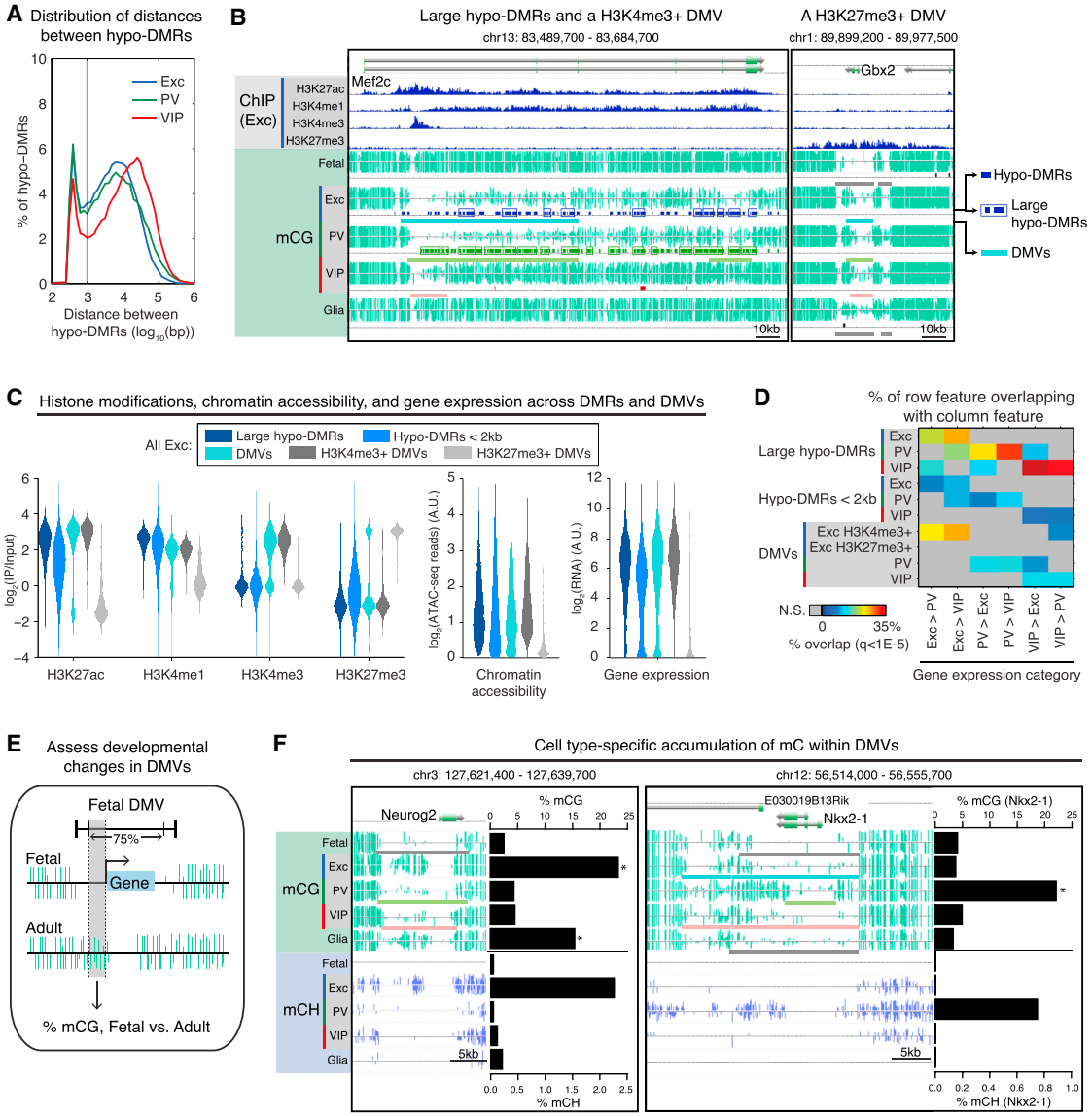

Figure 7. Large Domains of Low Methylation Link to Gene Expression, Including Unexpected Hyper-methylation at Developmental Genes

(A) Bimodal distribution of distances between hypo-DMRs in each cell type indicates that some hypo-DMRs are closely spaced (<1 kb separation) and form large blocks of differential methylation ("large hypo-DMRs").

(B) Large hypo-DMRs and an H3K4me3+ DNA methylation valley (DMV) overlap *Mef2c* (left); an H3K27me3+ DMV overlaps *Gbx2* (right). As diagrammed for the excitatory neuron tracks, dark-colored bars indicate hypo-DMRs (top), boxes indicate hypo-DMRs that were grouped into large hypo-DMRs, and light-colored bars indicate DMVs (bottom).

(C) For excitatory neurons, violin plots show the distribution of histone modification enrichments (left), ATAC-seq read densities (middle), and gene expression levels (right) within large hypo-DMRs, hypo-DMRs < 2 kb, and DMVs. A.U., arbitrary units.

(D) Matrix showing the percentage of each row feature that overlaps with differentially expressed genes. Large hypo-DMRs and H3K4me3+ DMVs (in excitatory neurons) have higher enrichment for differentially expressed genes, compared to hypo-DMRs < 2 kb. H3K27me3+ DMVs (in excitatory neurons) are not enriched for differentially expressed genes at $q < 1 \times 10^{-5}$.

(E) Schematic for assessing the accumulation of CG methylation in each adult cell type (excitatory, PV, and VIP neurons, and glia) compared to fetal cortex, at fetal DMVs overlapping genes. See Table S6.

(F) DNA methylation levels for a region around *Neurog2* (left), an active TF in excitatory and many glial progenitors, and *Nkx2-1* (right), a transiently active TF in PV neuron development. See Table S6 for annotations and references. Barplots show percentage of mCG and percentage of mCH for each cell type in the region between dotted lines in (E). *$q < 1 \times 10^{-10}$ (mCG, adult cell type compared to fetal cortex, one-sided FET with Benjamini-Hochberg correction). In the browser representation, light-colored bars indicate DMVs.

See also Figure S7.

EXPERIMENTAL PROCEDURES

Further details can be found in the Supplemental Experimental Procedures.

Mouse INTACT

Animal procedures were conducted in accordance with the Institutional Animal Care and Use Committee guidelines of the Johns Hopkins Medical Institutions. The *R26-CAG-LSL-Sun1-sfGFP-Myc* knockin mouse was made according to standard procedures. GFP+/Myc+ nuclei from adult (8–11 weeks) mouse neocortex were isolated by affinity purification using anti-GFP or anti-Myc antibodies and protein G-coated magnetic beads.

RNA-Seq Library Generation

Nuclear RNA from INTACT-purified nuclei or whole neocortical nuclei was converted to cDNA and amplified with the Nugen Ovation RNA-seq System V2 (Nugen 7102). Libraries were sequenced using the Illumina HiSeq 2500.

MethylC-Seq Library Generation

Genomic DNA from INTACT-purified nuclei was fragmented, and MethylC-seq libraries were prepared. Libraries were sequenced using the Illumina HiSeq 2000.

ATAC-Seq Library Generation

50,000 bead-bound nuclei were transposed using Tn5 transposase (Illumina FC-121-1030) as previously described (Buenrostro et al., 2013). After 9–12 cycles of PCR amplification, libraries were sequenced on an Illumina HiSeq 2500.

ChIP-Seq Library Generation

INTACT-purified excitatory neuron nuclei were digested to mononucleosomes using micrococcal nuclease, followed by salt extraction of chromatin. After native ChIP and library construction, libraries were sequenced on an Illumina HiSeq 2500.

ACCESSION NUMBERS

The accession number for the raw and processed data files reported in this paper is GEO: GSE63137, and the data files are displayed via a web-based browser (http://neomorph.salk.edu/mm_intact/).

SUPPLEMENTAL INFORMATION

Supplemental Information includes Supplemental Experimental Procedures, seven figures, and six tables and can be found with this article online at http://dx.doi.org/10.1016/j.neuron.2015.05.018.

AUTHOR CONTRIBUTIONS

J.N., J.R.E., S.R.E., and T.J.S. designed and supervised the research. A.M. designed and generated the INTACT mouse, developed the affinity purification, and did nuclei isolations and related experiments. G.L.H. designed the Sun1 tag and constructed RNA-seq libraries. G.L.H. and S.P. constructed ATAC-seq libraries. A.M. and G.L.H. constructed ChIP-seq libraries. S.P. sequenced the RNA-seq, ChIP-seq, and ATAC-seq libraries. M.A.U. constructed MethylC-seq libraries. J.R.N. sequenced and mapped the MethylC-seq libraries. E.A.M., F.P.D., C.L., A.M., and R.L. analyzed data. A.M., E.A.M., and J.N. prepared the manuscript. F.P.D., C.L., J.R.E., S.R.E., G.L.H., and R.L. revised the manuscript.

ACKNOWLEDGMENTS

This work was supported by the Howard Hughes Medical Institute (J.R.E., S.R.E., J.N., and T.J.S.), 1-U01-MH105985 (J.R.E.), MSTP training grant (A.M.), and NIH/NINDS R00NS080911 (E.A.M.). J.N. and T.J.S. are Howard Hughes Medical Institute Investigators. J.R.E. is a Howard Hughes Medical Institute and Gordon and Betty Moore Investigator. We thank Hao Zhang at the Johns Hopkins School of Public Health for flow cytometry. We thank Yupeng He for comments and suggestions.

Received: January 15, 2015
Revised: April 14, 2015
Accepted: May 7, 2015
Published: June 17 2015

REFERENCES

Amin, N.M., Greco, T.M., Kuchenbrod, L.M., Rigney, M.M., Chung, M.I., Wallingford, J.B., Cristea, I.M., and Conlon, F.L. (2014). Proteomic profiling of cardiac tissue by isolation of nuclei tagged in specific cell types (INTACT). Development *141*, 962–973.

Bird, A. (2002). DNA methylation patterns and epigenetic memory. Genes Dev. *16*, 6–21.

Buenrostro, J.D., Giresi, P.G., Zaba, L.C., Chang, H.Y., and Greenleaf, W.J. (2013). Transposition of native chromatin for fast and sensitive epigenomic profiling of open chromatin, DNA-binding proteins and nucleosome position. Nat. Methods *10*, 1213–1218.

Burger, L., Gaidatzis, D., Schübeler, D., and Stadler, M.B. (2013). Identification of active regulatory regions from DNA methylation data. Nucleic Acids Res. *41*, e155.

Deal, R.B., and Henikoff, S. (2010). A simple method for gene expression and chromatin profiling of individual cell types within a tissue. Dev. Cell *18*, 1030–1040.

DeFelipe, J., López-Cruz, P.L., Benavides-Piccione, R., Bielza, C., Larrañaga, P., Anderson, S., Burkhalter, A., Cauli, B., Fairén, A., Feldmeyer, D., et al. (2013). New insights into the classification and nomenclature of cortical GABAergic interneurons. Nat. Rev. Neurosci. *14*, 202–216.

Doyle, J.P., Dougherty, J.D., Heiman, M., Schmidt, E.F., Stevens, T.R., Ma, G., Bupp, S., Shrestha, P., Shah, R.D., Doughty, M.L., et al. (2008). Application of a translational profiling approach for the comparative analysis of CNS cell types. Cell *135*, 749–762.

Emmert-Buck, M.R., Bonner, R.F., Smith, P.D., Chuaqui, R.F., Zhuang, Z., Goldstein, S.R., Weiss, R.A., and Liotta, L.A. (1996). Laser capture microdissection. Science *274*, 998–1001.

Gabel, H.W., Kinde, B., Stroud, H., Gilbert, C.S., Harmin, D.A., Kastan, N.R., Hemberg, M., Ebert, D.H., and Greenberg, M.E. (2015). Disruption of DNA-methylation-dependent long gene repression in Rett syndrome. Nature. http://dx.doi.org/10.1038/nature14319.

Gay, L., Miller, M.R., Ventura, P.B., Devasthali, V., Vue, Z., Thompson, H.L., Temple, S., Zong, H., Cleary, M.D., Stankunas, K., and Doe, C.Q. (2013). Mouse TU tagging: a chemical/genetic intersectional method for purifying cell type-specific nascent RNA. Genes Dev. *27*, 98–115.

Gelman, D.M., and Marín, O. (2010). Generation of interneuron diversity in the mouse cerebral cortex. Eur. J. Neurosci. *31*, 2136–2141.

Gilsbach, R., Preissl, S., Grüning, B.A., Schnick, T., Burger, L., Benes, V., Würch, A., Bönisch, U., Günther, S., Backofen, R., et al. (2014). Dynamic DNA methylation orchestrates cardiomyocyte development, maturation and disease. Nat. Commun. *5*, 5288.

Guo, J.U., Ma, D.K., Mo, H., Ball, M.P., Jang, M.H., Bonaguidi, M.A., Balazer, J.A., Eaves, H.L., Xie, B., Ford, E., et al. (2011). Neuronal activity modifies the DNA methylation landscape in the adult brain. Nat. Neurosci. *14*, 1345–1351.

Guo, J.U., Su, Y., Shin, J.H., Shin, J., Li, H., Xie, B., Zhong, C., Hu, S., Le, T., Fan, G., et al. (2014). Distribution, recognition and regulation of non-CpG methylation in the adult mammalian brain. Nat. Neurosci. *17*, 215–222.

Heiman, M., Schaefer, A., Gong, S., Peterson, J.D., Day, M., Ramsey, K.E., Suárez-Fariñas, M., Schwarz, C., Stephan, D.A., Surmeier, D.J., et al. (2008). A translational profiling approach for the molecular characterization of CNS cell types. Cell *135*, 738–748.

Heintzman, N.D., Stuart, R.K., Hon, G., Fu, Y., Ching, C.W., Hawkins, R.D., Barrera, L.O., Van Calcar, S., Qu, C., Ching, K.A., et al. (2007). Distinct and

predictive chromatin signatures of transcriptional promoters and enhancers in the human genome. Nat. Genet. *39*, 311–318.

Henry, G.L., Davis, F.P., Picard, S., and Eddy, S.R. (2012). Cell type-specific genomics of Drosophila neurons. Nucleic Acids Res. *40*, 9691–9704.

Hobert, O., Carrera, I., and Stefanakis, N. (2010). The molecular and gene regulatory signature of a neuron. Trends Neurosci. *33*, 435–445.

Hon, G.C., Rajagopal, N., Shen, Y., McCleary, D.F., Yue, F., Dang, M.D., and Ren, B. (2013). Epigenetic memory at embryonic enhancers identified in DNA methylation maps from adult mouse tissues. Nat. Genet. *45*, 1198–1206.

Hovestadt, V., Jones, D.T., Picelli, S., Wang, W., Kool, M., Northcott, P.A., Sultan, M., Stachurski, K., Ryzhova, M., Warnatz, H.J., et al. (2014). Decoding the regulatory landscape of medulloblastoma using DNA methylation sequencing. Nature *510*, 537–541.

Huang, W., Sherman, B.T., and Lempicki, R.A. (2009). Systematic and integrative analysis of large gene lists using DAVID bioinformatics resources. Nat. Protoc. *4*, 44–57.

Jeong, M., Sun, D., Luo, M., Huang, Y., Challen, G.A., Rodriguez, B., Zhang, X., Chavez, L., Wang, H., Hannah, R., et al. (2014). Large conserved domains of low DNA methylation maintained by Dnmt3a. Nat. Genet. *46*, 17–23.

Jiang, Y., Matevossian, A., Huang, H.S., Straubhaar, J., and Akbarian, S. (2008). Isolation of neuronal chromatin from brain tissue. BMC Neurosci. *9*, 42.

Kepecs, A., and Fishell, G. (2014). Interneuron cell types are fit to function. Nature *505*, 318–326.

Kessaris, N., Magno, L., Rubin, A.N., and Oliveira, M.G. (2014). Genetic programs controlling cortical interneuron fate. Curr. Opin. Neurobiol. *26*, 79–87.

Kim, T.K., Hemberg, M., Gray, J.M., Costa, A.M., Bear, D.M., Wu, J., Harmin, D.A., Laptewicz, M., Barbara-Haley, K., Kuersten, S., et al. (2010). Widespread transcription at neuronal activity-regulated enhancers. Nature *465*, 182–187.

Lister, R., O'Malley, R.C., Tonti-Filippini, J., Gregory, B.D., Berry, C.C., Millar, A.H., and Ecker, J.R. (2008). Highly integrated single-base resolution maps of the epigenome in Arabidopsis. Cell *133*, 523–536.

Lister, R., Mukamel, E.A., Nery, J.R., Urich, M., Puddifoot, C.A., Johnson, N.D., Lucero, J., Huang, Y., Dwork, A.J., Schultz, M.D., et al. (2013). Global epigenomic reconfiguration during mammalian brain development. Science *341*, 1237905.

Malik, A.N., Vierbuchen, T., Hemberg, M., Rubin, A.A., Ling, E., Couch, C.H., Stroud, H., Spiegel, I., Farh, K.K., Harmin, D.A., and Greenberg, M.E. (2014). Genome-wide identification and characterization of functional neuronal activity-dependent enhancers. Nat. Neurosci. *17*, 1330–1339.

Maze, I., Shen, L., Zhang, B., Garcia, B.A., Shao, N., Mitchell, A., Sun, H., Akbarian, S., Allis, C.D., and Nestler, E.J. (2014). Analytical tools and current challenges in the modern era of neuroepigenomics. Nat. Neurosci. *17*, 1476–1490.

Mellén, M., Ayata, P., Dewell, S., Kriaucionis, S., and Heintz, N. (2012). MeCP2 binds to 5hmC enriched within active genes and accessible chromatin in the nervous system. Cell *151*, 1417–1430.

Molyneaux, B.J., Arlotta, P., Menezes, J.R., and Macklis, J.D. (2007). Neuronal subtype specification in the cerebral cortex. Nat. Rev. Neurosci. *8*, 427–437.

Molyneaux, B.J., Goff, L.A., Brettler, A.C., Chen, H.H., Brown, J.R., Hrvatin, S., Rinn, J.L., and Arlotta, P. (2015). DeCoN: genome-wide analysis of in vivo transcriptional dynamics during pyramidal neuron fate selection in neocortex. Neuron *85*, 275–288.

Neph, S., Vierstra, J., Stergachis, A.B., Reynolds, A.P., Haugen, E., Vernot, B., Thurman, R.E., John, S., Sandstrom, R., Johnson, A.K., et al. (2012). An expansive human regulatory lexicon encoded in transcription factor footprints. Nature *489*, 83–90.

Nóbrega-Pereira, S., Kessaris, N., Du, T., Kimura, S., Anderson, S.A., and Marín, O. (2008). Postmitotic Nkx2-1 controls the migration of telencephalic interneurons by direct repression of guidance receptors. Neuron *59*, 733–745.

Rashid, A.J., Cole, C.J., and Josselyn, S.A. (2014). Emerging roles for MEF2 transcription factors in memory. Genes Brain Behav. *13*, 118–125.

Rudy, B., Fishell, G., Lee, S., and Hjerling-Leffler, J. (2011). Three groups of interneurons account for nearly 100% of neocortical GABAergic neurons. Dev. Neurobiol. *71*, 45–61.

Sanz, E., Yang, L., Su, T., Morris, D.R., McKnight, G.S., and Amieux, P.S. (2009). Cell-type-specific isolation of ribosome-associated mRNA from complex tissues. Proc. Natl. Acad. Sci. USA *106*, 13939–13944.

Saxena, A., Wagatsuma, A., Noro, Y., Kuji, T., Asaka-Oba, A., Watahiki, A., Gurnot, C., Fagiolini, M., Hensch, T.K., and Carninci, P. (2012). Trehalose-enhanced isolation of neuronal sub-types from adult mouse brain. Biotechniques *52*, 381–385.

Sommer, L., Ma, Q., and Anderson, D.J. (1996). neurogenins, a novel family of atonal-related bHLH transcription factors, are putative mammalian neuronal determination genes that reveal progenitor cell heterogeneity in the developing CNS and PNS. Mol. Cell. Neurosci. *8*, 221–241.

Spiegel, I., Mardinly, A.R., Gabel, H.W., Bazinet, J.E., Couch, C.H., Tzeng, C.P., Harmin, D.A., and Greenberg, M.E. (2014). Npas4 regulates excitatory-inhibitory balance within neural circuits through cell-type-specific gene programs. Cell *157*, 1216–1229.

Stadler, M.B., Murr, R., Burger, L., Ivanek, R., Lienert, F., Schöler, A., van Nimwegen, E., Wirbelauer, C., Oakeley, E.J., Gaidatzis, D., et al. (2011). DNA-binding factors shape the mouse methylome at distal regulatory regions. Nature *480*, 490–495.

Stamatoyannopoulos, J.A., Snyder, M., Hardison, R., Ren, B., Gingeras, T., Gilbert, D.M., Groudine, M., Bender, M., Kaul, R., Canfield, T., et al.; Mouse ENCODE Consortium (2012). An encyclopedia of mouse DNA elements (Mouse ENCODE). Genome Biol. *13*, 418.

Steiner, F.A., Talbert, P.B., Kasinathan, S., Deal, R.B., and Henikoff, S. (2012). Cell-type-specific nuclei purification from whole animals for genome-wide expression and chromatin profiling. Genome Res. *22*, 766–777.

Sugino, K., Hempel, C.M., Miller, M.N., Hattox, A.M., Shapiro, P., Wu, C., Huang, Z.J., and Nelson, S.B. (2006). Molecular taxonomy of major neuronal classes in the adult mouse forebrain. Nat. Neurosci. *9*, 99–107.

Sullivan, P.F., Daly, M.J., and O'Donovan, M. (2012). Genetic architectures of psychiatric disorders: the emerging picture and its implications. Nat. Rev. Genet. *13*, 537–551.

Teif, V.B., Beshnova, D.A., Vainshtein, Y., Marth, C., Mallm, J.P., Höfer, T., and Rippe, K. (2014). Nucleosome repositioning links DNA (de)methylation and differential CTCF binding during stem cell development. Genome Res. *24*, 1285–1295.

Thurman, R.E., Rynes, E., Humbert, R., Vierstra, J., Maurano, M.T., Haugen, E., Sheffield, N.C., Stergachis, A.B., Wang, H., Vernot, B., et al. (2012). The accessible chromatin landscape of the human genome. Nature *489*, 75–82.

Verzi, M.P., Agarwal, P., Brown, C., McCulley, D.J., Schwarz, J.J., and Black, B.L. (2007). The transcription factor MEF2C is required for craniofacial development. Dev. Cell *12*, 645–652.

Visel, A., Taher, L., Girgis, H., May, D., Golonzhka, O., Hoch, R.V., McKinsey, G.L., Pattabiraman, K., Silberberg, S.N., Blow, M.J., et al. (2013). A high-resolution enhancer atlas of the developing telencephalon. Cell *152*, 895–908.

Wang, B., Long, J.E., Flandin, P., Pla, R., Waclaw, R.R., Campbell, K., and Rubenstein, J.L. (2013). Loss of Gsx1 and Gsx2 function rescues distinct phenotypes in Dlx1/2 mutants. J. Comp. Neurol. *521*, 1561–1584.

Xie, W., Barr, C.L., Kim, A., Yue, F., Lee, A.Y., Eubanks, J., Dempster, E.L., and Ren, B. (2012). Base-resolution analyses of sequence and parent-of-origin dependent DNA methylation in the mouse genome. Cell *148*, 816–831.

Xie, W., Schultz, M.D., Lister, R., Hou, Z., Rajagopal, N., Ray, P., Whitaker, J.W., Tian, S., Hawkins, R.D., Leung, D., et al. (2013). Epigenomic analysis of multilineage differentiation of human embryonic stem cells. Cell *153*, 1134–1148.

Yu, M., Hon, G.C., Szulwach, K.E., Song, C.X., Zhang, L., Kim, A., Li, X., Dai, Q., Shen, Y., Park, B., et al. (2012). Base-resolution analysis of 5-hydroxymethylcytosine in the mammalian genome. Cell *149*, 1368–1380.